Dynamics of optical excitations in a Fe/MgO(001) heterostructure from time-dependent density functional theory

Markus Ernst Gruner* and Rossitza Pentcheva†
Faculty of Physics and Center for Nanointegration, CENIDE, University of Duisburg-Essen, 47048 Duisburg, Germany

(Received 18 January 2019; revised manuscript received 13 March 2019; published 2 May 2019)

In the framework of real-time time-dependent density functional theory we unravel the layer-resolved dynamics of excited carriers in a $(Fe)_1/(MgO)_3(001)$ multilayer after an optical excitation with a frequency below the band gap of bulk MgO. Substantial transient changes to the electronic structure, which persist after the duration of the pulse, are mainly observed for in-plane polarized electric fields, corresponding to a laser pulse arriving perpendicular to the interface. While the strongest charge redistribution takes place in the Fe layer, a time-dependent change in the occupation numbers is visible in all layers, mediated by the presence of interface states. The time evolution of the layer-resolved time-dependent occupation numbers indicates a strong orbital dependence with the depletion from in-plane orbitals (e.g., $d_{x^2-y^2}$ of Fe) and accumulation in out-of-plane orbitals ($d_{3z^2-r^2}$ of Fe and p_z of apical oxygen). We also observe a small net charge transfer of less than one percent of an electron away from oxygen towards the Mg sites, even for MgO layers which are not directly in contact with the metallic Fe.

DOI: 10.1103/PhysRevB.99.195104

I. INTRODUCTION

Resolving the impact of optical excitations on the different degrees of freedom present in solid-state materials on ultrashort time scales provides important insight in the coupling mechanisms present in modern functional materials. This is relevant for the preparation of novel transient states of matter, which cannot be reached in an ergodic process under equilibrium conditions but can be accessed through the excitation with a strong laser pulse [1–4]. Such questions are addressed in pump-probe experiments using optical or x-ray pulses with femto- or picosecond delay. A large fraction of these experiments are devoted to resolving and controlling the dynamics of magnetization reversal processes [5,6] (for an overview, see also Ref. [7] and references therein) and the particular dynamics of spin and orbital moments in metals [8]. Furthermore, the spin-relaxation time of hot carriers in Au was studied in an optical-pump second-optical-harmonic probe experiment on a Au/Fe/MgO(001) multilayer stack [9]. Another outstanding example is the investigation of the dynamics of the electronic structure in the laser-induced insulator-to-metal transition in VO_2 [10].

From a theoretical point of view, time-dependent density functional theory (TDDFT) has evolved to a major workhorse in describing the excitation of molecules and extended systems by laser pulses (for recent reviews, see, e.g., Refs. [11–14]). For weak laser pulses, linear-response TDDFT (LR-TDDFT) with an appropriately chosen exchange-correlation kernel can provide an adequate description of the frequency-dependent excitation spectrum [15]. For strong pulses, where nonlinear effects become relevant, real-time TDDFT (RT-TDDFT) approaches based on the explicit solution of the time-dependent Kohn-Sham equations with an external time-dependent electrical potential need to be employed. The high computational demand limits the system size, but increasing computing power and ongoing code development help to overcome the limitations. A large fraction of TDDFT calculations is concerned with zero-dimensional systems, such as molecules or clusters (e.g., Refs. [16–19]). More recently, also bulk systems are addressed with RT-TDDFT, for instance, to disentangle the demagnetization processes in metals [20–22] or to describe light-matter interaction in semiconductors [23–25], including the numerical simulation of pump-probe experiments in Si [26]. Increasingly, also time-dependent processes in complex systems were investigated, such as reactions at surfaces [27,28], magnetic transitions in metal multilayers [29,30], or ultrafast charge-transfer dynamics in van der Waals coupled dichalcogenide layers [31–33].

Interfaces are ubiquitous in many of the above materials, as these are grown on substrates or designed as multilayer systems. These may decisively influence the dynamics and dissipation of optical excitations. Therefore the spatial propagation of excited carriers through an interface can be considered as an important fundamental research question. In the present work, we will concentrate on a system consisting of a metallic part and a wide-band-gap insulator. We have selected the paradigmatic system Fe/MgO(001), for which the electronic and transport properties have been intensively studied in the past [34–44] due to its relevance for spintronics applications as a tunneling magnetoresistive element in hard disk read heads [45,46] or spin diode or rectifier for magnetic logic elements [47]. The choice of the system was also motivated by recent optical-pump, x-ray-probe experiments, where the optical-pump pulse was designed to excite the metallic subsystem only [48].

The purpose of the present work is to explore with RT-TDDFT under which conditions an optically induced elec-

*Markus.Gruner@uni-due.de
†Rossitza.Pentcheva@uni-due.de

tronic excitation may propagate into and possibly through the interface. Due to the high computational cost of this method, we concentrate here on a minimal heterostructure containing a single Fe layer and three layers of MgO, i.e., $Fe_1/(MgO)_3(001)$. We consider laser pulses with a frequency which is lower than the band gap of MgO but sufficiently large to excite electrons in Fe to a level close to or above the conduction-band minimum of MgO. Our main focus is then on the temporal and spacial evolution of electronic density and orbital polarization as a function of the laser pulse polarization direction and frequency.

The paper is structured as follows: After a presentation of the computational details in Sec. II, a brief discussion of the ground-state geometry and electronic structure of the $Fe_1/(MgO)_3(001)$ heterostructure is given in Sec. III A. In Sec. III B, we discuss the strongly anisotropic frequency-dependent properties of the system, which are related to the imaginary part of the dielectric tensor obtained with LR-TDDFT. Section III C reports the real-time evolution of the electronic system following an excitation with optical pulses as a function of frequency and polarization direction. Finally, the results are summarized in Sec. IV.

II. COMPUTATIONAL DETAILS

The ground-state properties (lattice parameters and atomic positions) were obtained with the VASP plane-wave code [49] (version 5.4.4) using the generalized gradient approximation (GGA) by Perdew, Burke, and Ernzerhof (PBE) for exchange and correlation [50] with a plane-wave cutoff of 500 eV. We employed potentials with the valence configuration $2s^2 2p^4$ for O, $3s^2$ for Mg, and $3d^7 4s^1$ for Fe, constructed for use with the projector augmented wave method (PAW) [51]. Brillouin zone integration was carried out on a $12 \times 12 \times 4$ k mesh with Gaussian-type Fermi-surface smearing ($\sigma = 0.1$ eV). Convergence criteria for the electronic self-consistency cycle and for internal position and lattice parameters are 10^{-7} and 10^{-5} eV, respectively. Since we are not primarily interested in magnetization dynamics, spin-orbit coupling was not considered in our calculations.

The electronic structure, optical absorption spectra, and time evolution after optical excitation were calculated with the previously optimized geometry using the ELK full-potential augmented plane-wave code [52]. For consistency with the real-time calculations we have selected the local density approximation (LDA) for the exchange-correlation functional of Perdew and Wang (PW92) [53]. Site-resolved density of states and magnetic moments are in close agreement with the VASP calculations using PBE. A cutoff parameter $RK_{\max} = 7$ for the plane waves and a maximum angular momentum $l_{\max} = 7$ for the PAW functions was used in combination with Fermi-type smearing, corresponding to an electronic temperature of $T = 316$ K and muffin-tin radii of 1.139 Å for Fe, 1.164 Å for Mg, and 0.855 Å for O. Convergence criterion for electronic self-consistency was a root-mean-square change of 10^{-7} in the Kohn-Sham potential.

The dynamic evolution of an optical excitation was calculated with TDDFT in the real-time (RT) domain using adiabatic LDA (ALDA), which is local in space and time. We used a $8 \times 8 \times 3$ mesh in reciprocal space and the above-mentioned technical parameters. The time propagation was carried out for at least 42 fs, discretized with a time step of 0.1 a.u. $= 2.419 \times 10^{-18}$ s. The numerical stability of the time evolution was tested in an additional run without an externally applied laser pulse, confirming that the system remains in its initial state. The laser pulse was modeled by a time-dependent but spatially constant vector potential $\vec{A}(t)$, which contributes to the kinetic energy in the time-dependent Kohn-Sham equations in terms of the generalized momentum operator $\vec{p} = -\frac{i\hbar}{m_e}\nabla + \frac{e_0}{c}\vec{A}(t)$. We simulated laser pulses with different frequencies. In all cases, the waves were convoluted with a Gaussian with FWHM of 5.81 fs, which corresponds to an effective peak time of 11.6 fs. Finally, we scaled the amplitudes to obtain a constant peak power density of 4.2 TW/cm^2 for all pulses. Multiplied with the FWHM, this yields a laser fluence of 25 mJ/cm^2, which is a typical magnitude in pump-probe experiments [54,55].

The dynamic changes of the occupation numbers during and after applying a laser pulse were monitored by the time-dependent spectral function $D(E,t)$, see Ref. [29]. The spin-resolved $D_\sigma(E,t)$ is calculated from the projection of the time-propagated orbitals $\Phi(\vec{r},t)_{j\vec{k}\sigma}$ onto the ground-state Kohn-Sham orbitals at $t = 0$, which can be used to define time-dependent and spin-resolved occupation numbers (with spin index σ):

$$g_{i\vec{k}\sigma}(t) = \sum_j n_{j\vec{k}\sigma} \left| \int d^3r\, \Phi_{j\vec{k}\sigma}(\vec{r},t) \Phi^*_{i\vec{k}\sigma}(\vec{r},0) \right|^2. \quad (1)$$

These are associated with the energies corresponding to the respective orbitals in the ground state and integrated over the Brillouin zone (BZ), obtaining the expression

$$D_\sigma(E,t) = \sum_i \int_{\mathrm{BZ}} d^3k\, \delta(E - \epsilon_{i\vec{k}\sigma})\, g_{i\vec{k}\sigma}(t). \quad (2)$$

For the following discussion it is important to keep in mind that $D_\sigma(E,t)$ is used here as an effective tool to visualize the change in the occupation of particular orbitals; differences between features in $D_\sigma(E,t)$ do not necessarily correspond to real excitation energies.

The frequency-dependent dielectric function was calculated in the framework of the random phase approximation (RPA) in the limit $q \to 0$, neglecting microscopic contributions. We compared these results with LR-TDDFT, taking into account many-body effects with the "bootstrap" (BS) exchange-correlation kernel [56], which includes self-consistently optimized long-range corrections. These calculations were carried out with a $16 \times 16 \times 6$ k mesh for $Fe_1/(MgO)_3(001)$, 32^3 k points for bulk Fe, and 48^3 k points for bulk MgO.

III. RESULTS

A. Geometry and electronic structure

While the possibility of a FeO layer formation at the interface has also been addressed [58–62], most of the studies of Fe/MgO heterostructures use sharp interfaces [34,42,57]. In our approach we adopted the latter model, having O located apically to the Fe [34,42,57], as this configuration shows the lowest interface energy [63]. The superlattice consists of one

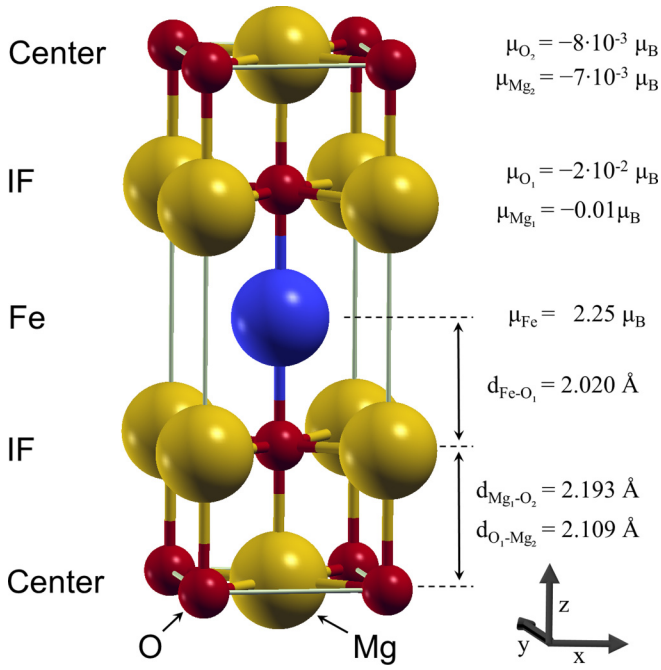

FIG. 1. Unit cell of the four-layer $Fe_1/(MgO)_3(001)$ heterostructure, consisting of one Fe layer, the central MgO, and one MgO interface layer (IF) after structural optimization ($a = b = 2.972$ Å, $c = 8.432$ Å). The numbers indicate the magnetic moments in the muffin-tin spheres obtained from ELK (LDA).

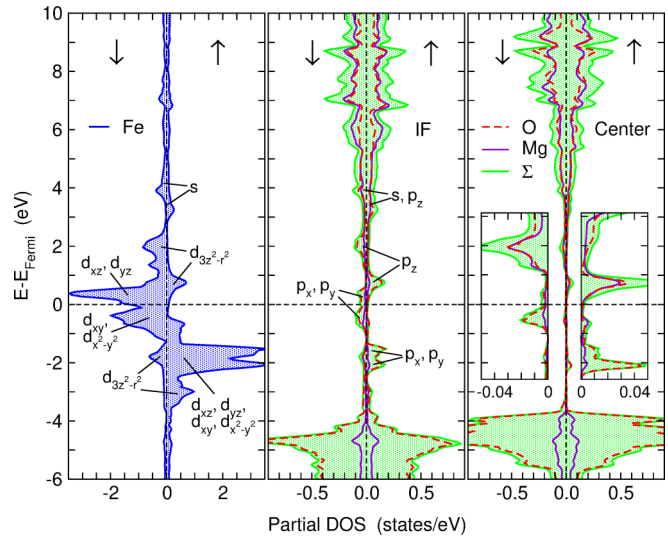

FIG. 2. Spin-resolved layer-resolved electronic partial density of states (PDOS) of $Fe_1(MgO)_3(001)$ obtained with ELK (LDA). The left panel shows the Fe-projected PDOS (blue lines), the center and right panel the PDOS from Mg, O, and their sum (Σ) in the IF and center layer, respectively. Here, red dashed lines correspond to the O-projected PDOS, while solid violet lines mark the contribution from Mg. Their sum is indicated by the green lines and background. For Fe and O (IF), additional labels indicate the orbitals which predominantly contribute to selected important features.

Fe layer and three layers of bulk MgO. The optimized cell parameters for the structure shown in Fig. 1 are $c = 8.259$ Å and $a = b = 2.954$ Å, indicating a reasonable lattice mismatch of -3.1 % for MgO and $+4.4$ % for Fe, compared to the lattice constants of the respective bulk systems obtained with similar technical settings. The distance between interface (IF) O and Fe is 2.020 Å, while the MgO (IF) layer turns out to be slightly corrugated: the distance between the central Mg and O (IF) amounts to 2.109 Å, whereas the one between Mg (IF) and central O is slightly larger, 2.193 Å, in agreement with earlier studies [58,64,65]. Using ELK for the optimization of the atomic positions, we obtain a very similar result [66]; with ELK, Mg (IF) and O (IF) move slightly closer to the Fe plane. The variation of the z-component difference to the VASP (PBE) result is 0.009 Å for Fe-Mg and 0.010 Å for Fe-O within ELK-PBE and 0.008 Å for Fe-Mg and 0.030 Å for Fe-O within ELK-LDA, retaining the corrugation of the IF layer for both codes and functionals. The magnetic moment of Fe is 2.25 μ_B, close to the value for bulk bcc-Fe. On the other hand, thicker Fe films in Fe/MgO(001) exhibit enhanced magnetic moments (not shown here), consistent with previous first-principles theory [64,67,68] and experiment [69–71]. Owing to the reduced dimensions, the bandwidth of the single Fe layer is significantly narrowed compared to bulk Fe (cf. projected density of states in Fig. 2, left panel). The Fermi level is now pinned in a dip in the minority spin density of states (DOS) between the predominantly occupied d_{xy} and $d_{x^2-y^2}$ orbitals around -0.5 eV and the unoccupied d_{xz} and d_{yz} at $+0.3$ eV. The hybridization of Fe with the apical O leads to broadening and splitting of the majority spin $d_{3z^2-r^2}$ band into bonding and antibonding contributions centered at -3 and $+1$ eV, respectively. The pseudogap in the majority channel close to the Fermi level and the finite DOS in the minority spin channel imply a significant spin dependence of the transport properties for the $Fe_1/(MgO)_3(001)$ heterostructure. The correspondence of the peaks in the Fe- and MgO partial DOS (PDOS) in the adjacent interface (IF) layer (middle panel of Fig. 2) indicates strong hybridization between Fe and O states in the energy range between –3 and +3 eV. The sharp peaks in the Fe PDOS at around –2 eV in the majority channel and around –0.4 and +0.3 eV in the minority channel, which result from d orbitals with in-plane orientation, coincide with the positions of p_x and p_y states of O (IF). Likewise, we see marked features with p_z character at +0.8 and +2 eV above the Fermi level, which are the result from the strong hybridization with the out-of-plane $d_{3z^2-r^2}$ orbitals of Fe. The features at +0.3, +0.8, and +2 eV turn out to be of particular importance for the optical excitation discussed in in Sec. III C. The energy range below –3 eV and above +3 eV, particularly in the central MgO layer (the right panel of Fig. 2), resembles bulk MgO. Still, some hybridization effects, for instance, the p_z features above the Fermi level, are visible in the central layer, indicating that the interface region extends to deeper MgO layers. Nevertheless, the correspondence to the DOS of bulk MgO enables us to estimate the band alignment at the Fe/MgO interface within the local density and generalized gradient approximations used here. We note that LDA and GGA exchange-correlation functionals severely underestimate the band gap of MgO, which can affect the band alignment. Using LDA with the same technical parameters as in our TDDFT setup at the experimental bulk lattice constant, the direct MgO gap at Γ amounts to 4.64 eV, compared to

the experimental value of 7.7 eV [72–74]. The size of the band gap can be corrected by using hybrid functionals or many-body perturbation theory using the GW approximation (e.g., Refs. [75–77]) and the Bethe-Salpeter equation (BSE) that are beyond the scope of the present investigation.

It is not straightforward to identify the position of the bulk MgO gap in the heterostructure. Interface states, as discussed above, arise from the hybridization with orbitals originating from the metal layers. These decay exponentially in the MgO layers, as, e.g., shown in Ref. [78] for a Si/SiO_2 interface. In addition, one may also consider a change of the gap due to quantum confinement effects. Epitaxial strain arising from the combination of different materials also affects the band structure. One could infer from the right panel of Fig. 2, which shows the valence-band maximum in the central layer about 3.7 eV below the Fermi level, that the conduction-band minimum of MgO should be located between 1.0 and 1.5 eV above E_F. Consequently, the p_x, p_y, and p_z interface states of O (IF) just above E_F would essentially lie within the gap, whereas the second p_z interface state at +2.0 eV would already be within the conduction band. A projection of the bulk band structure of MgO calculated in the same Brillouin zone onto the bands of the $Fe_1/(MgO)_3(001)$ heterostructure (not shown) indeed reveals a good match with the valence-band maximum of MgO at Γ with the Fe/MgO bands around −3.72 eV. Above the Fermi level, bands with significant Mg and O character at Γ at about 1.20 and 2.15 eV can be associated with the lowest conduction bands of bulk MgO. Naturally, the band alignment depends also on the thickness of the slabs. For comparison, in the $Fe_8/(MgO)_8(001)$ heterostructure investigated in Ref. [48] the valence-band maximum of the central layer is located at –3.34 eV, while states at Γ which may be associated with the conduction-band minimum of the MgO slab are encountered at 1.67 and 1.85 eV.

B. Absorption spectra from linear-response TDDFT

The optical properties of the heterostructure are reflected in the frequency-dependent dielectric tensor $\epsilon(\omega)$, which can be derived from the electronic structure in terms of the frequency-dependent Kohn-Sham susceptibility. We calculated the imaginary part $\mathrm{Im}[\epsilon(\omega)]$, which describes the absorption of the material, within the RPA and also with TDDFT in the linear-response scheme. We compare $\mathrm{Im}[\epsilon(\omega)]$ of the $Fe_1/(MgO)_3(001)$ heterostructure with the respective bulk systems, i.e., bcc-Fe and rocksalt MgO, see Fig. 3. The bulk results agree well with the results of previous calculations [79–82] obtained within the same level of approximation. For metallic Fe, including the microscopic contributions from the exchange-correlation kernel does not notably alter the results, even with long-range corrections. In contrast, the "bootstrap" kernel (BS) leads to a significant renormalization of the optical absorption spectrum for the insulating bulk MgO, which strongly improves the agreement with experiment at larger excitation energies, whereas the appropriate description of the strong excitonic peak at 7.7 eV requires many-body perturbation theory involving the Bethe-Salpeter equation [76,80,82].

Due to the broken symmetry in z direction, the difference between the in-plane (ϵ_{xx} and ϵ_{yy}, upper panel) and out-of-plane (ϵ_{zz}, lower panel) components of the dielectric tensor indicates a substantial dependence on the polarization of the incident light wave. The in-plane components of the imaginary part of the dielectric tensor resemble (apart from a factor 2 in magnitude) the respective quantity of bcc Fe, with a large absorption in the low-energy region. This corresponds to the setup where the incident light wave arrives perpendicular to the absorbing Fe layers. In contrast, the frequency dependence of the out-of-plane component $\mathrm{Im}[\epsilon_{zz}(\omega)]$ bears similarity to $\mathrm{Im}[\epsilon(\omega)]$ of bulk MgO, where absorption takes place only for photon energies above the gap. In the $Fe_1/(MgO)_3(001)$ heterostructure, the band alignment of MgO with metallic Fe and the presence of IF states below and above E_F arising from hybridization causes weak absorption in the entire energy range below 4.7 eV.

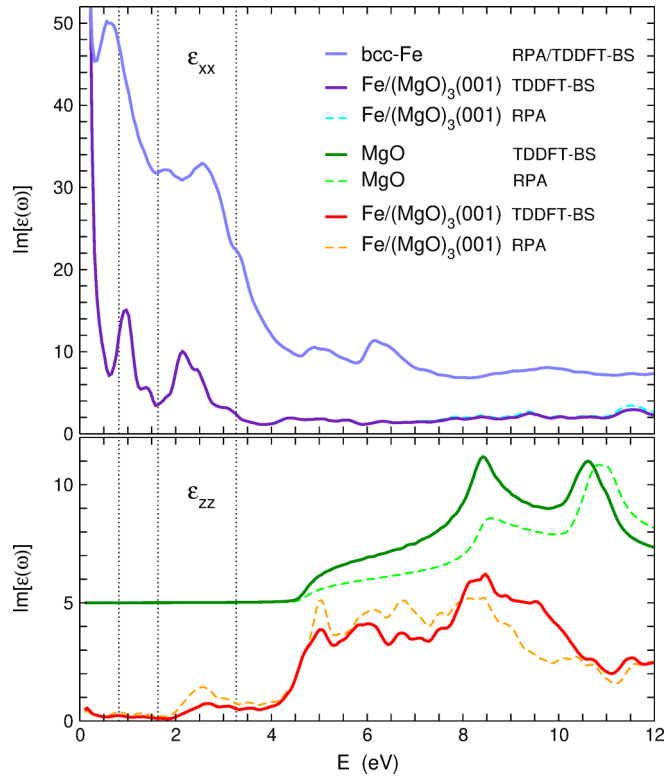

FIG. 3. Frequency dependence of the imaginary part of the dielectric tensor $\mathrm{Im}[\epsilon_{ij}(\omega)]$ in the $Fe_1/(MgO)_3(001)$ heterostructure obtained with ELK within the random phase approximation (RPA) and LR-TDDFT, with the "bootstrap" (TDDFT-BS) exchange-correlation kernel. The upper panel shows the in-plane components $\mathrm{Im}[\epsilon_{xx}(\omega)] = \mathrm{Im}[\epsilon_{yy}(\omega)]$ and the out-of-plane component $\mathrm{Im}[\epsilon_{zz}(\omega)]$. The $\mathrm{Im}[\epsilon_{xx}(\omega)]$ bears similarity with $\mathrm{Im}[\epsilon(\omega)]$ of bulk Fe, while $\mathrm{Im}[\epsilon_{zz}(\omega)]$ resembles bulk MgO. The spectra of bulk Fe and MgO are shifted vertically by a constant value of 5 for clarity. The vertical lines denote the laser frequencies used in our RT-TDDFT calculations.

Taking into account many-body effects in the framework of the bootstrap exchange-correlation kernel [56] apparently does not make a substantial difference for metallic Fe and accordingly, also the in-plane components in our $Fe_1/(MgO)_3(001)$ heterostructure. For bulk MgO, the bootstrap kernel causes a downward shift and rearrangement of the features at 8.5 and 11 eV as compared to RPA. For the

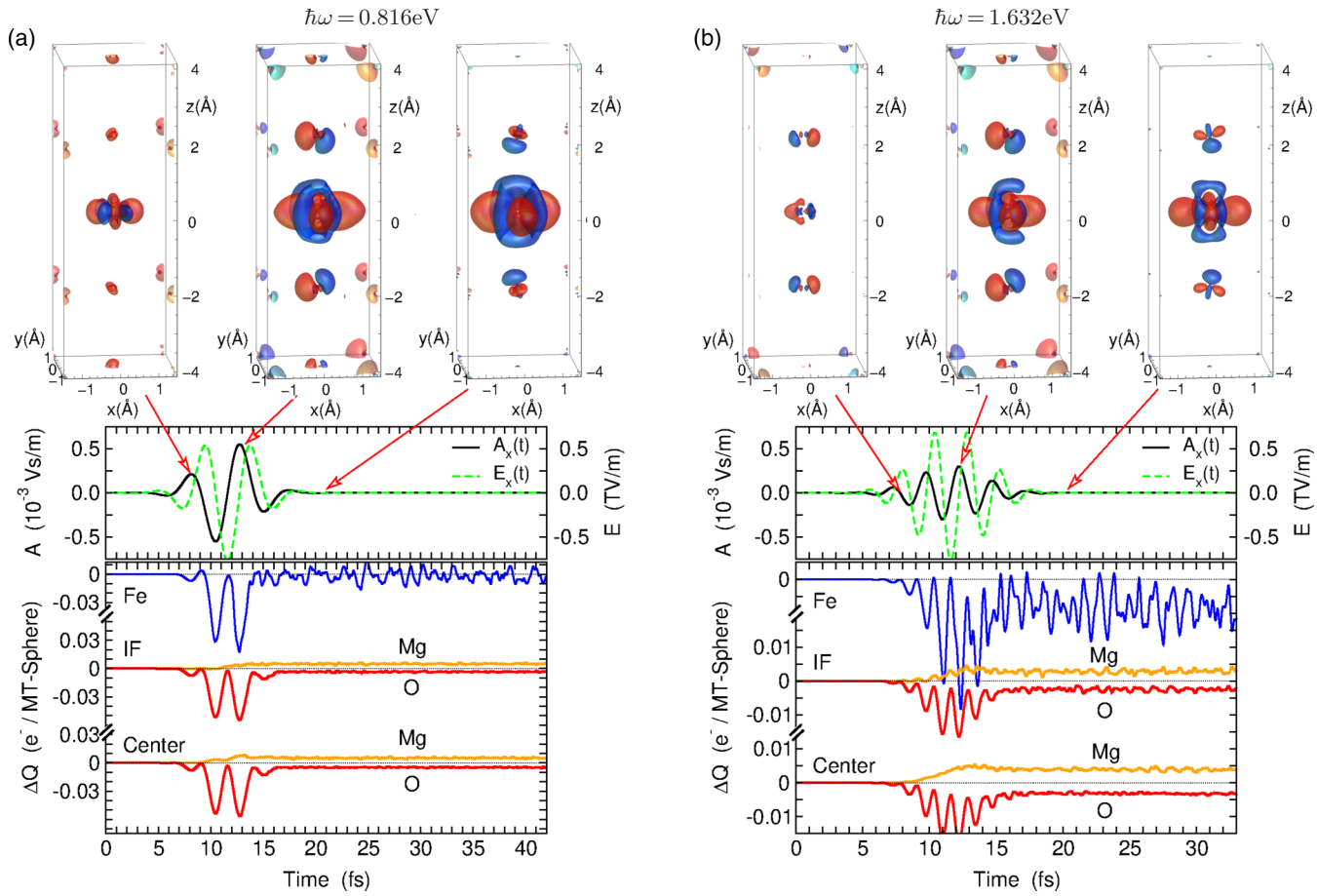

FIG. 4. Time evolution of the charge distribution during a laser pulse with frequency (a) $\hbar\omega = 0.816$ eV and (b) $\hbar\omega = 1.632$ eV. The upper panels show the change in electronic density $\rho(\vec{r}, t)$ relative to the initial state $\rho(\vec{r}, t) - \rho(\vec{r}, 0)$ in terms of isosurfaces corresponding to charge levels of $\pm 2 \times 10^{-3}\, e_0/a_B^3$ at three different points in time ($t = 8.1$, 11.8, and 20 fs). Red color denotes a depletion of electronic (negative) charge, blue an accumulation inside the isosurface. The panels in the central row represent the time dependence of the external vector field $\vec{A}(t) = A_x \vec{e}_x$ (solid black line) and the resulting electric field $\vec{E}(t) = -\partial\vec{A}/\partial t$ (dashed green line). The lower panels depict the time-dependent change in the electronic charge $\Delta Q = Q(t) - Q(0)$ residing inside the muffin-tin spheres of Fe, Mg, and O in the different layers.

out-of-plane $\mathrm{Im}[\epsilon_{zz}(\omega)]$ $Fe_1/(MgO)_3(001)$, we rather notice a redistribution of spectral weight in opposite direction for the TDDFT calculations compared to the RPA.

C. Real-time evolution of optical excitations

To investigate the dynamics of excitation and charge transfer into and across the interface, we chose three different frequencies for optical excitations, $\hbar\omega = 0.816$, 1.632, and 3.265 eV, while keeping the laser fluence constant. All three excitations are clearly within the gap of bulk MgO; thus a direct excitation from the valence band to the conduction band cannot take place. However, the band alignment in our heterostructure suggests that the conduction-band edge of MgO is located between 1.2 and 2.2 eV above the Fermi level, as discussed in Sec. III A. Thus the lower frequency produces excitations in Fe with final states predominantly below the conduction-band edge of MgO, while with $\hbar\omega = 1.632$ eV one can already address states in the central layer which correspond to the conduction band of MgO. For completeness, we considered a third energy, $\hbar\omega = 3.265$ eV, which clearly reaches Fe states above the conduction-band minimum of MgO, while a direct excitation of carriers between states corresponding to the MgO valence and conduction band is still inhibited. Besides the frequency dependence, we explore the effect of different polarization directions of the incoming light wave.

1. In-plane polarization

In a typical setup in pump-probe experiments, the laser pulse propagates normal to the sample surface. The electrical field components are then confined within the x-y plane. Figure 4(a) presents the evolution of the charge distribution during and after an in-plane polarized laser pulse of $\hbar\omega = 0.816$ eV. While this energy is not yet sufficient to reach the MgO conduction band in the heterostructure, Fig. 4(b) shows the corresponding results for a pulse with $\hbar\omega = 1.632$ eV, where the transfer of an excitation to the conduction band minimum of the central MgO layer is possible. Apart from the smaller amplitude of the charge fluctuation [cf. the lower panel of Fig. 4(b)], the electric field causes a rather analogous response in both cases. The upper panels visualize snapshots of the electron density redistribution at $t = 8.2$, 11.9, and

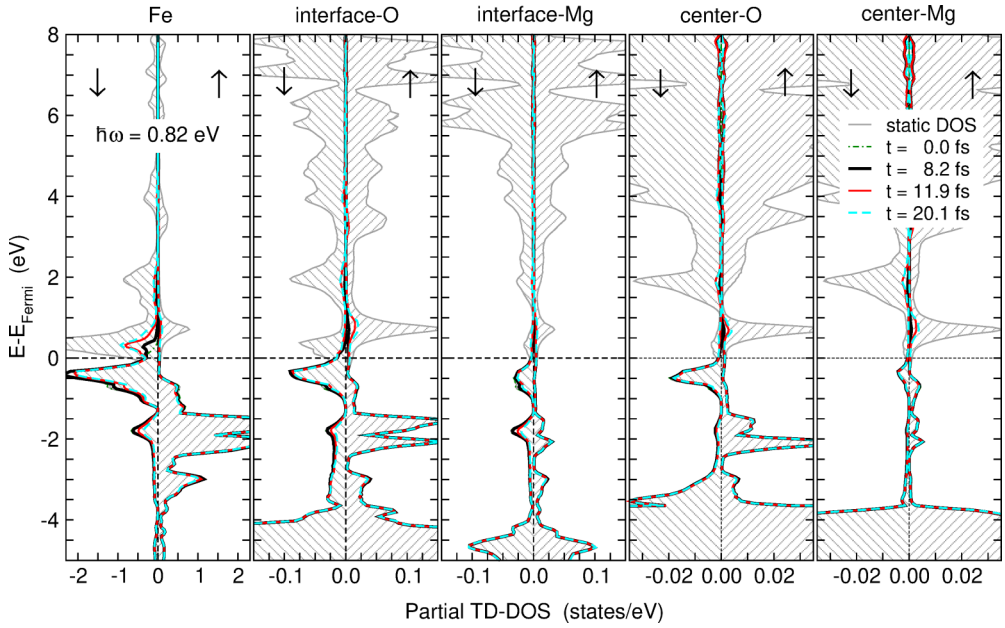

FIG. 5. Site-resolved time-dependent partial spectral function $D_\sigma(E,t)$ for $\hbar\omega = 0.816$ eV evaluated at four different points in time, corresponding to the snapshots in the charge density in Fig. 4(a): $t = 0$ (thin dash-dotted line), $t = 8.2$ fs (thick black line), $t = 11.9$ fs (thick red line), and $t = 20.1$ fs (thick dashed cyan line). The gray hatched areas in the background show the corresponding static partial DOS obtained from a ground-state calculation with the same technical settings.

20.1 fs which correspond to the onset of the pulse, the largest amplitude of the vector potential, and after the decay of the laser pulse, respectively. Our results show that the redistribution is strongest around the Fe sites but affects the whole MgO region. At the onset of the pulse, charge dipoles form particularly at Fe and the apical O sites and to a lesser extent also at the Mg and central O sites. At the Fe site, the redistribution of charge exhibits a strong orbital dependence: charge is depleted essentially from the in-plane d orbitals (d_{xy}, $d_{x^2-y^2}$) and accumulated in out-of-plane orbitals ($d_{3z^2-r^2}$, d_{xz}, d_{yz}). Similarly, an accumulation is observed in the p_z orbital of the apical oxygen. The oscillation of the electrical field in x direction forces the dipoles around the apical O to rotate with the accumulated (blue) electron bulb always located between the O and Fe sites. With decreasing field strength the redistribution of charge largely regresses, particularly in the central layer and at Mg (IF). The prominent features at the Fe and the apical O (IF) sites remain, finally reaching a steady, weakly oscillating state. (An animation of the time-dependent evolution of the charge distribution is provided as Supplemental Material [83].)

The integrated charge contained in the muffin-tin spheres centered around each lattice site shown in the lower panels of Fig. 4 renders a complementary view of the dynamical evolution of the charge distribution. During the pulse, the electric field accelerates the electronic charge which temporarily leaves the muffin-tin spheres. When the field reaches its negative turning point, the charge is largely restored. This picture is encountered only for the Fe and O spheres, which harbor a significant amount of valence charge as opposed to Mg. The reduction of charge at Fe and O sites starts at approximately $t = 7$ fs, while a much smaller accumulation in the Mg spheres is encountered later, at $t = 9$ fs. Since the total charge in the system is conserved, we conclude that with each oscillation of the field, charge subsequently swashes out of the O and Fe spheres into the interstitial, from where a fraction eventually moves into the positively charged Mg spheres. Thus, the light field effectively pumps electronic charge from the O towards the Mg sites. Interestingly, the behavior of the IF and central layer is qualitatively similar but differs in magnitude, due to the fact that the central MgO layer of this thin heterostructure has not yet reached bulk optical properties. This effect remains stationary even after the laser pulse has been switched off.

Further insight into the evolution of the electronic structure can be obtained from the spin- and site-resolved time-dependent spectral function $D_\sigma(E,t)$, shown in Fig. 5 for $\hbar\omega = 0.816$ eV for distinct times t. At $t = 0$ all states below E_F are occupied, apart from the thermal broadening. With time evolving, excitations build up in particular in the minority spin channel of Fe, 0.3 eV above the Fermi level, obviously fostered by the availability of d_{xz} and d_{yz} states. A similar trend can be observed at the $d_{3z^2-r^2}$ peak at 0.75 eV in the majority channel. Since this peak is much smaller, the effects are not as pronounced and barely visible in Fig. 5. However, they become apparent if we look on a magnified scale at the corresponding hybridized IF states of the apical O atoms. Compared to O (IF), we encounter a significantly smaller response from the states above the Fermi level for Mg (IF). In the central layer the change in occupation numbers is significantly smaller but still visible. In contrast to the IF, the center Mg response is rather similar to O.

For a detailed analysis of the temporal evolution of the electronic structure after the onset of the laser pulse, we use the time-dependent changes in the spectral weight of the occupied states (ΔTDDOS), defined as the difference of the time-resolved spectral function $\Delta D_\sigma(E,t)$ at time t with respect to the initial state, i.e., $D_\sigma(E,t) - D_\sigma(E,0)$. The

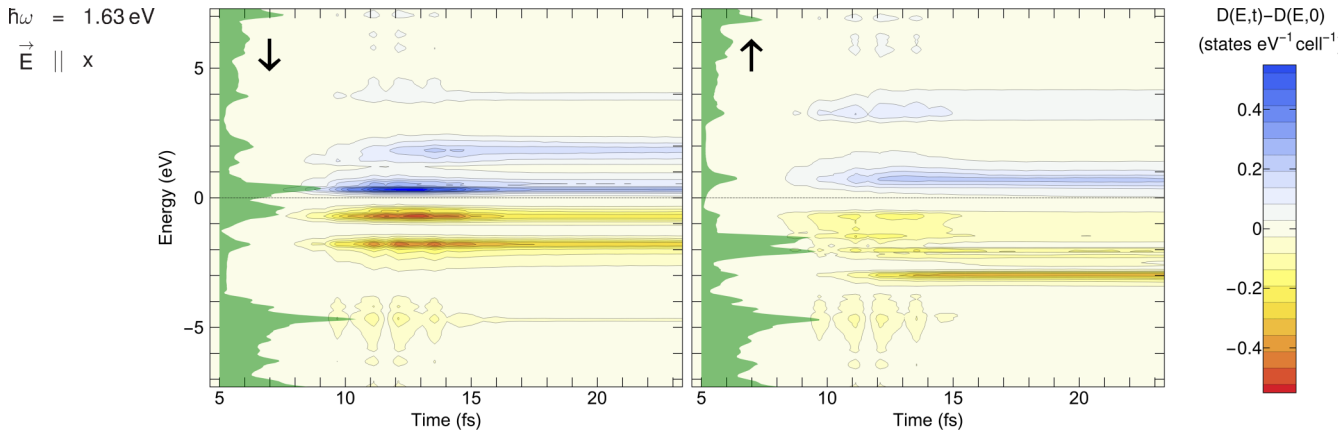

FIG. 6. Energy- and time-resolved changes in the ΔTDDOS, $\Delta D_\sigma(E,t) = D_\sigma(E,t) - D_\sigma(E,0)$ for the laser pulse shown in Fig. 4(b) ($\hbar\omega = 1.632$ eV). The left panel refers to the minority spin channel, the right panel to the majority spin channel. Orange and red colors refer to a depletion of occupation, blue colors to an increase. The green area at the left edge of each panel indicates the shape of the spin-resolved total density of states.

contour plot of the total ΔTDDOS in Fig. 6 for the case $\hbar\omega = 1.632$ eV exhibits distinct features which are directly correlated to regions of high density of states of Fe in the respective spin channel (cf. Fig. 2 and the green area in each panel of Fig. 6). Independent of the laser energy, the minority channel exhibits the largest ΔTDDOS, as the peaks in the ground-state majority DOS are generally smaller in the vicinity of E_F. Here, the largest changes occur during the pulse; afterwards we see an essentially stationary picture, keeping in mind that relaxation processes beyond the electronic time scale are not accounted for in the current RT-TDDFT modeling.

We observe the fastest response to the laser pulse in the energy range closest to the Fermi level, whereas the change in occupation appears retarded for the more distant states. We interpret this as a signature of a secondary excitation process, where previously created holes below E_F are refilled by electrons originating from a lower-lying state. Multiple subsequent excitations might also account for the rather strong depletion of the d states close to -2 eV (minority channel) and -3 eV (majority channel) for $\hbar\omega = 1.632$ eV.

The isolated features, which appear in particular at low and high energies (below -4 eV and above $+4$ eV) far beyond the excitation energy of the laser correlate to the extrema of the vector potential. Here, the electric field has its largest contribution to the generalized momentum of the electrons, which directly impacts their kinetic energy. Therefore, we ascribe these effects to a partially nonlinear response arising from the large amplitude of the laser field in combination with the comparatively broad frequency distribution in our Gaussian-shaped finite-length pulses. The features decay quickly with decreasing vector potential, but a small persistent change in occupation may remain, even after the pulse is over.

We now address the dynamic evolution of the site- and orbital-resolved partial ΔTDDOS, which we compare in Fig. 7 for the three laser frequencies. We selected the Fe-3d and the sum of the Mg-2p and O-2p orbitals (the latter resolved for IF and center layers) which provide the largest contributions for the respective layers. The Fe-d contribution is the largest in absolute numbers and thus closely resembles the time evolution of the total spectral function. This confirms that the light predominately interacts with the d electrons of the Fe layer. In accordance with our calculation of the frequency-dependent dielectric tensor (Fig. 3 in Sec. III B), we find a considerably weaker interaction (absorption) of the laser field with the electronic structure for increasing laser frequencies. (Note the change in the scale of the contour plots in Fig. 7, where the distance between two contour lines is reduced from the top to the bottom panels.)

Concentrating on the IF-MgO (center panels in Fig. 7), we observe a particularly strong occupation of the O-p_z states above the Fermi level (+0.8 eV in the majority channel and +2 eV in the minority channel) which are present at these energies due to the hybridization with the Fe-$d_{3z^2-r^2}$ states. In relation to the excitation taking place in the Fe layer, these contributions become considerably more pronounced with increasing laser frequency. In turn, we find a much weaker occupation of the O-p_x and p_y orbitals above E_F, as we would expect from the size of the peaks in the static DOS in Fig. 2. In contrast to the p_z orbitals, their ΔTDDOS strongly decreases with energy and nearly vanishes at $\hbar\omega = 3.265$ eV. Below E_F, there is a considerable depletion of the in-plane p orbitals, which is again a consequence of the hybridization with the in-plane Fe-3d orbitals. As for the IF layer, we find the largest ΔTDDOS of the states at +0.8 eV (majority channel) and +2 eV (minority channel) in the central layer, which now results from both O and Mg (cf. Fig. 5). In contrast, however, we do not observe a similar depletion of the states below E_F. We find mainly additional occupation of particular states above E_F without concomitant deoccupation of corresponding states below, which we would expect in case of a direct excitation within the layer. Therefore, our observation might rather be considered as a signature of excitations propagating into the interface, and we can infer that—in contrast to the in-plane orbitals—hybridization between the out-of-plane orbitals at the interface, i.e., Fe-$d_{3z^2-r^2}$ and O-p_z, are of particular importance for the propagation of excitations into deeper MgO layers away from the interface. Since the O-p_z states in the minority channel are located above the conduction-band edge, the excitation may even propagate into bulk MgO. This aspect needs further investigation, since it can be affected by the

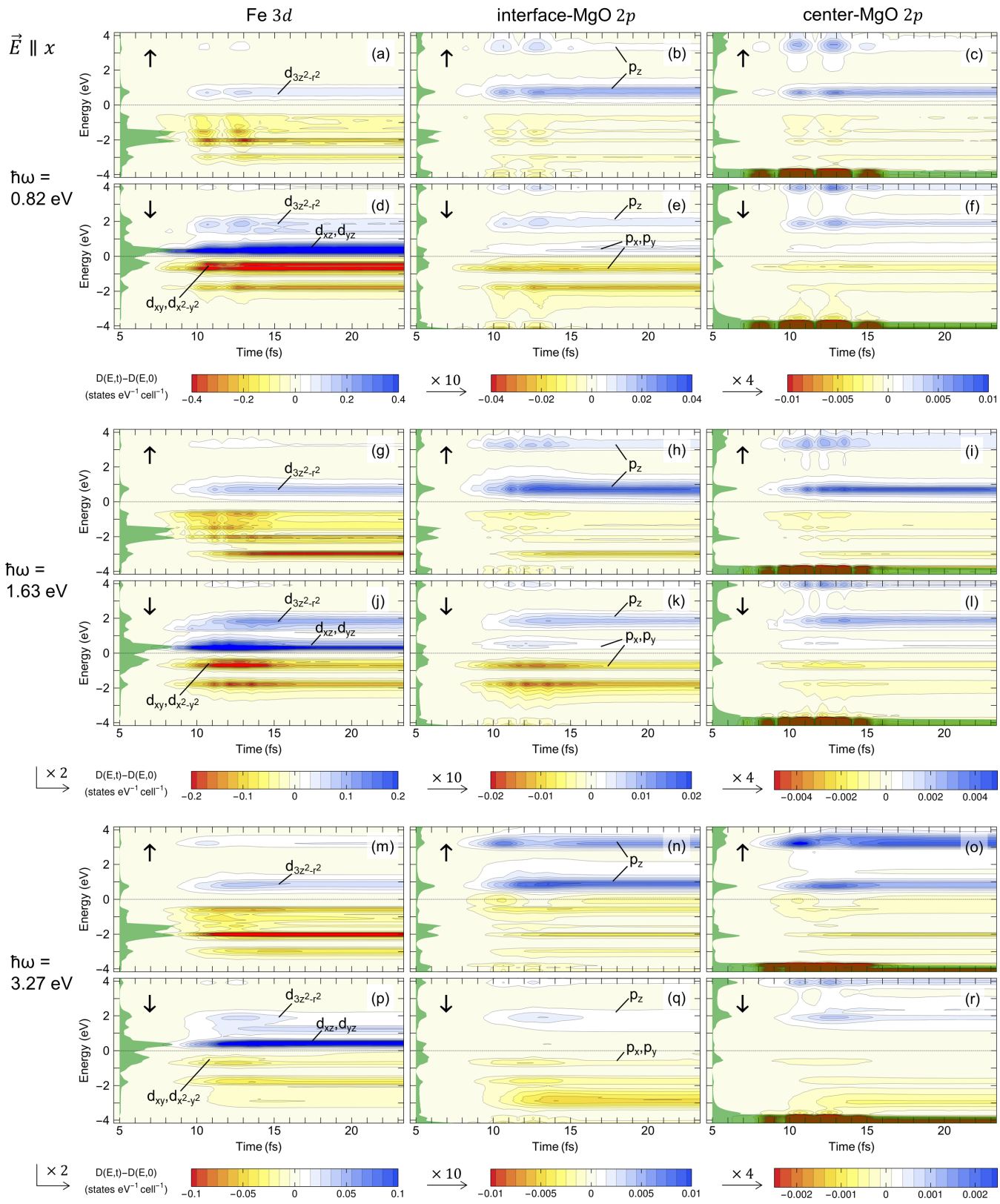

FIG. 7. Energy- and time-resolved changes in the atom- and orbital-resolved ΔTDDOS for the laser frequencies (a)–(d) $\hbar\omega = 0.816$ eV, (g)–(l) $\hbar\omega = 1.632$ eV, and (m)–(r) $\hbar\omega = 3.265$ eV. The left column refers to the Fe-3d states, the middle column to the IF-MgO-2p states, and the right column to the center-MgO-2p states. Note that the scale of the color coding (and the static partial DOS indicated by the green area) changes between the panels.

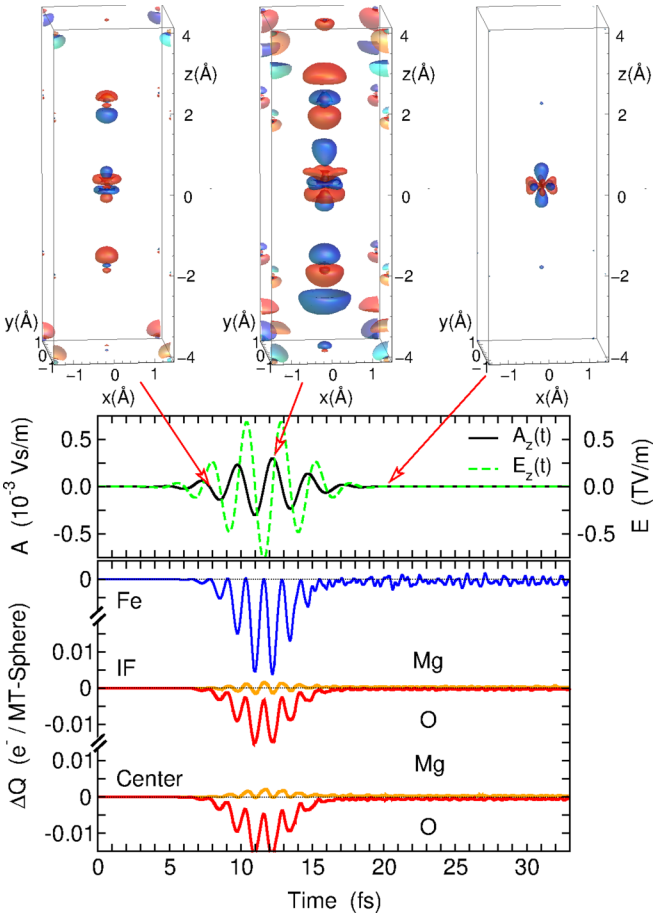

FIG. 8. Time evolution of the charge distribution during a laser pulse with frequency $\hbar\omega = 1.632$ eV with out-of-plane polarization of the vector field $\vec{A}(t) = A_z \vec{e}_z$. Same colors and lines as in Fig. 4.

underestimation of the MgO band gap within LDA and the thickness of the MgO region.

2. *Cross-plane polarized pulse*

A qualitatively different response is obtained when the polarization of the vector potential is in out-of-plane direction, which we briefly discuss here for the frequency $\hbar\omega = 1.632$ eV. As illustrated by Figs. 8 and 9, the charge clouds around the atoms now oscillate in vertical direction, which leads again to a decrease of charge inside the muffin-tin spheres of Fe and O, comparable to the respective in-plane case. The time evolution of the charge density shows that persistent excitations remain beyond 20 fs, but these are essentially located at the Fe site (Fig. 8). In contrast to the in-plane polarized pulse, we do not encounter a significant persistent charge transfer from O to Mg. From the time dependence of the occupation numbers in Fig. 9 we conclude that the charge redistribution at the Fe site is mainly related to a redistribution of states in the minority channel across the Fermi level, which occurs only in an interval of ± 0.5 eV around E_F. As in the in-plane case, we also see strong changes in $D_\sigma(E,t)$ at the maximum of the vector potential. Most of these features vanish, however, when the pulse is over. This means that a permanent absorption of photons has not taken place in this case. We infer from the absence of strong transient changes after the laser pulse that the cross-plane electric field component of a laser pulse arriving at a grazing angle will not contribute substantially to the excitation process in and across the interface. The distinct behavior for in- and out-of-plane polarization is consistent with the anisotropic behavior of the imaginary part of the dielectric tensor discussed in Sec. III B.

IV. CONCLUSIONS

We simulate the excitation of a metal-insulator heterostructure by an ultrashort laser pulse in the visible and infrared frequency range with real-time TDDFT, revealing the dynamic evolution of electronic excitations at the interface. We consider an ultrathin $Fe_1/(MgO)_3(001)$ heterostructure and photon energies which are below the band gap of bulk MgO but sufficient for a local excitation in the Fe layer, which subsequently could induce an electronic transfer into the conduction band of MgO. Furthermore, we identify the prominent role of the interface states to propagate the excitation into the MgO with a dominant contribution of the out of plane orbitals.

We observe that excitations and their possible propagation through the system take place nearly instantaneously, i.e.,

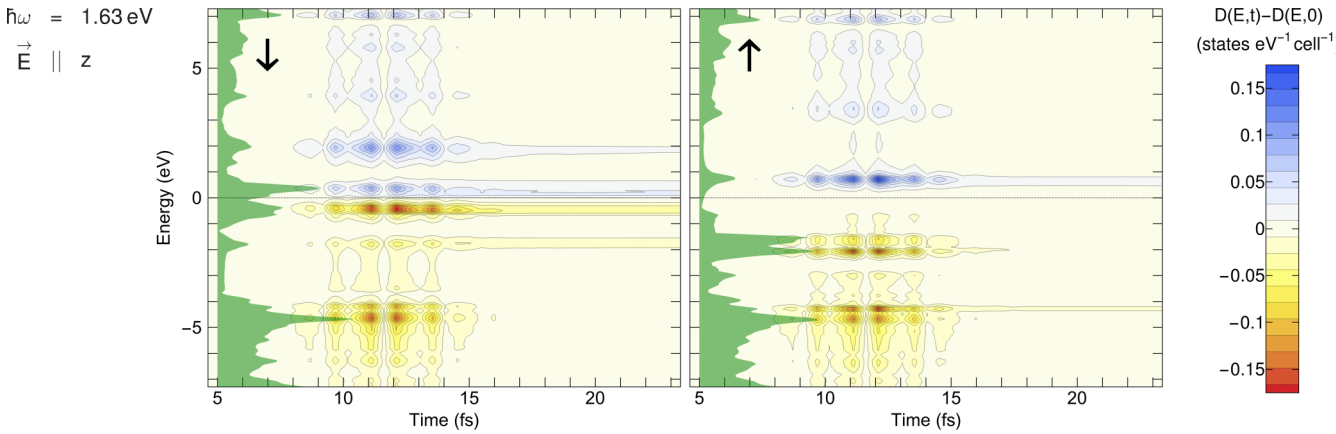

FIG. 9. Energy- and time-resolved changes in the total ΔTDDOS $D_\sigma(E,t) - D_\sigma(E,0)$ for the laser pulse shown in Fig. 8. Same colors and symbols as in Fig. 6.

during the laser pulse. After the pulse, the system reaches an essentially stationary state which remains unaltered up to at least 42 fs. For normal incidence, when the electric field of the laser light is polarized within the Fe plane, we observe particularly strong accumulations in states which arise from the hybridization of the p_z orbitals of O with the $d_{3z^2-r^2}$ orbitals of Fe at the interface. In the central layer, which has no direct contact to Fe, we still find states within the gap which share this particular sensitivity to the light pulse. We consider this as a strong indication that hybridization of orbitals which are oriented along z (i.e., in cross-plane direction) is of particular importance to inject excitations across the interface into deeper layers. We further observe a weak charge transfer from O to Mg in the interface but also in the central MgO layer. For cross-plane polarization, strong effects are confined to the duration of the pulse; the steady state involves mainly the Fe layer. Charge transfer from O to Mg and persistent laser-induced excitation of states above the Fermi level are suppressed.

Using in-plane polarized light, a heterostructure with favorably hybridized orbitals might thus potentially be used for the optical injection of carriers with a specific spin-polarization into the conduction band of a semiconductor or insulator, whereas the out-of-plane component does not contribute to this process substantially. The dependence on the light polarization direction is understood based on the frequency-dependent dielectric tensor calculated using LR-TDDFT, which involves a strong anisotropy. The imaginary part of the xx component implies significant absorption, resembling $\mathrm{Im}[\epsilon_{xx}]$ of bulk Fe. In turn, the zz component rather bears similarities to the optical response of MgO, but we still find a small but finite absorption in $\mathrm{Im}[\epsilon_{zz}]$ in the low-frequency range due to the interface states.

Our minimal model system gives a first comprehensive overview on the fundamental response of a metal-insulator heterostructure after a laser excitation, while future work shall address more realistic heterostructures with thicker slabs and many-body effects [75–77] that are currently not available in RT-TDDFT.

ACKNOWLEDGMENTS

We gratefully acknowledge discussions with Sangeeta Sharma (MPI Berlin), Peter Elliot (MPI Halle), Andrea Eschenlohr, Uwe Bovensiepen, Heiko Wende, and Klaus Sokolowski-Tinten (University of Duisburg-Essen). This work was funded by the Deutsche Forschungsgemeinschaft (DFG, German Research Foundation) through Project No. 278162697 – SFB 1242, Subproject No. C02. Calculations were carried out on the MagnitUDE supercomputer system (DFG Grants No. INST 20876/209-1 FUGG and No. INST 20876/243-1 FUGG).

[1] R. Ernstorfer, M. Harb, C. T. Hebeisen, G. Sciaini, T. Dartigalongue, and R. J. D. Miller, Science **323**, 1033 (2009).
[2] S. Ichikawa, H. Nozawa, T. Sato, A. Tomita, K. Ichiyanagi, M. Chollet, L. Guerin, N. Dean, A. Cavalleri, S. Adachi, T. Arima, H. Sawa, Y. Ogimoto, M. Nakamura, R. Tamaki, K. Miyano, and S. Koshihara, Nat. Mater. **10**, 101 (2011).
[3] L. Stojchevska, I. Vaskivskyi, T. Mertelj, P. Kusar, D. Svetin, S. Brazovskii, and D. Mihailovic, Science **344**, 177 (2014).
[4] H. Hübener, M. A. Sentef, U. De Giovanni, A. F. Kemper, and A. Rubio, Nat. Commun. **8**, 13940 (2017).
[5] C. Stamm, T. Kachel, N. Pontius, R. Mitzner, T. Quast, K. Holldack, S. Khan, C. Lupulescu, E. F. Aziz, M. Wietstruk, H. A. Dürr, and W. Eberhardt, Nat. Mater. **6**, 740 (2007).
[6] I. Radu, K. Vahaplar, C. Stamm, T. Kachel, N. Pontius, H. A. Dürr, T. A. Ostler, J. Barker, R. F. L. Evans, R. W. Chantrell, A. Tsukamoto, A. Itoh, A. Kirilyuk, T. Rasing, and A. V. Kimel, Nature (London) **472**, 205 (2011).
[7] A. Eschenlohr and U. Bovensiepen, J. Phys.: Condens. Matter **30**, 030301 (2018).
[8] C. Boeglin, E. Beaurepaire, V. Halté, V. López-Flores, C. Stamm, N. Pontius, H. A. Dürr, and J.-Y. Bigot, Nature (London) **465**, 458 (2010).
[9] A. Melnikov, I. Razdolski, T. O. Wehling, E. T. Papaioannou, V. Roddatis, P. Fumagalli, O. Aktsipetrov, A. I. Lichtenstein, and U. Bovensiepen, Phys. Rev. Lett. **107**, 076601 (2011).
[10] A. Cavalleri, M. Rini, H. H. W. Chong, S. Fourmaux, T. E. Glover, P. A. Heimann, J. C. Kieffer, and R. W. Schoenlein, Phys. Rev. Lett. **95**, 067405 (2005).
[11] S. Botti, A. Schindlmayr, R. Del Sole, and L. Reining, Rep. Prog. Phys. **70**, 357 (2007).
[12] *Fundamentals of Time-Dependent Density Functional Theory*, edited by M. A. L. Marques, N. T. Maitra, F. M. S. Nogueira, E. K. U. Gross, and A. Rubio, Lecture Notes in Physics (Springer, Berlin/Heidelberg, 2012), Vol. 837.
[13] S. Sharma, J. K. Dewhurst, and E. K. U. Gross, Top. Curr. Chem. **347**, 235 (2014).
[14] V. Olevano, TDDFT, excitations, and spectroscopy: Applications to optical, electron and X-ray spectroscopy, in *Structures on Different Time Scales* (De Gruyter, Berlin/Boston, 2018), pp. 101–142.
[15] N. T. Maitra, J. Chem. Phys. **144**, 220901 (2016).
[16] K. Burke, J. Werschnik, and E. K. U. Gross, J. Chem. Phys. **123**, 062206 (2005).
[17] Y. Takimoto, F. D. Vila, and J. J. Rehr, J. Chem. Phys. **127**, 154114 (2007).
[18] K. Lopata and N. Govind, J. Chem. Theory Comput. **7**, 1344 (2011).
[19] C. Cocchi, D. Prezzi, A. Ruini, E. Molinari, and C. A. Rozzi, Phys. Rev. Lett. **112**, 198303 (2014).
[20] K. Krieger, J. K. Dewhurst, P. Elliott, S. Sharma, and E. K. U. Gross, J. Chem. Theory Comput. **11**, 4870 (2015).
[21] P. Elliott, T. Müller, J. K. Dewhurst, S. Sharma, and E. K. U. Gross, Sci. Rep. **6**, 38911 (2016).
[22] K. Krieger, P. Elliot, T. Müller, N. Singh, J. K. Dewhurst, E. K. U. Gross, and S. Sharma, J. Phys.: Condens. Matter **29**, 224001 (2017).
[23] S. A. Sato, Y. Shinohara, T. Otobe, and K. Yabana, Phys. Rev. B **90**, 174303 (2014).
[24] N. Tancogne-Dejean, O. D. Mücke, F. X. Kärtner, and A. Rubio, Nat. Commun. **8**, 745 (2017).

[25] P. D. Pemmaraju, F. D. Vila, J. J. Kas, S. A. Sato, J. J. Rehr, and K. Yabana, Comput. Phys. Commun. **226**, 30 (2018).

[26] S. A. Sato, K. Yabana, Y. Shinohara, T. Otobe, and G. F. Bertsch, Phys. Rev. B **89**, 064304 (2014).

[27] M. Grotemeyer and E. Pehlke, in *Dynamics of Gas-Surface Interactions*, edited by R. Diez Muiño and H. F. Busnego, Springer Series in Surface Science (Springer, Berlin/Heidelberg, 2013), Vol. 50, Chap. 12, p. 299.

[28] Y. Miyamoto, H. Zhang, X. Cheng, and A. Rubio, Phys. Rev. B **96**, 115451 (2017).

[29] J. K. Dewhurst, P. Elliott, S. Shallcross, E. K. U. Gross, and S. Sharma, Nano Lett. **18**, 1842 (2018).

[30] J. Chen, U. Bovensiepen, A. Eschenlohr, T. Müller, P. Elliott, E. K. U. Gross, J. K. Dewhurst, and S. Sharma, Phys. Rev. Lett. **122**, 067202 (2019).

[31] H. Wang, J. Bang, Y. Sun, L. Liang, D. West, V. Meunier, and S. Zhang, Nat. Commun. **7**, 11504 (2016).

[32] Z. Ji, H. Hong, J. Zhang, Q. Zhang, W. Huang, T. Cao, R. Qiao, C. Liu, J. Liang, C. Jin, L. Jiao, K. Shi, S. Meng, and K. Liu, ACS Nano **11**, 12020 (2017).

[33] B. Buades, A. Picón, I. León, N. Di Palo, S. L. Cousin, C. Cocchi, E. Pellegrin, J. H. Martin, S. Mañas Valero, E. Coronado, T. Danz, C. Draxl, M. Uemoto, K. Yabana, M. Schultze, S. Wall, and J. Biegert, arXiv:1808.06493.

[34] W. H. Butler, X.-G. Zhang, T. C. Schulthess, and J. M. MacLaren, Phys. Rev. B **63**, 054416 (2001).

[35] J. Mathon and A. Umerski, Phys. Rev. B **63**, 220403(R) (2001).

[36] C. Tiusan, J. Faure-Vincent, C. Bellouard, M. Hehn, E. Jouguelet, and A. Schuhl, Phys. Rev. Lett. **93**, 106602 (2004).

[37] D. Waldron, V. Timoshevskii, Y. Hu, K. Xia, and H. Guo, Phys. Rev. Lett. **97**, 226802 (2006).

[38] K. D. Belashchenko, J. Velev, and E. Y. Tsymbal, Phys. Rev. B **72**, 140404(R) (2005).

[39] C. Heiliger, P. Zahn, B. Y. Yavorsky, and I. Mertig, Phys. Rev. B **77**, 224407 (2008).

[40] J. Peralta-Ramos, A. M. Llois, I. Rungger, and S. Sanvito, Phys. Rev. B **78**, 024430 (2008).

[41] I. Rungger, O. Mryasov, and S. Sanvito, Phys. Rev. B **79**, 094414 (2009).

[42] X. Feng, O. Bengone, M. Alouani, S. Lebègue, I. Rungger, and S. Sanvito, Phys. Rev. B **79**, 174414 (2009).

[43] B. Abedi Ravan, A. A. Shokri, and A. Yazdani, Solid State Commun. **150**, 214 (2010).

[44] T. Z. Raza, J. I. Cerdá, and H. Raza, J. Appl. Phys. **109**, 023705 (2011).

[45] S. S. P. Parkin, C. Kaiser, A. Panchula, P. M. Rice, B. Hughes, M. Samant, and S.-H. Yang, Nat. Mater. **3**, 862 (2004).

[46] S. Yuasa, T. Nagahama, A. Fukushima, Y. Suzuki, and K. Ando, Nat. Mater. **3**, 868 (2004).

[47] A. Iovan, S. Andersson, Y. G. Naidyuk, A. Vedyaev, B. Dieny, and V. Korenivski, Nano Lett. **8**, 805 (2008).

[48] N. Rothenbach, M. E. Gruner, K. Ollefs, C. Schmitz-Antoniak, S. Salamon, P. Zhou, R. Li, M. Mo, S. Park, X. Shen, S. Weathersby, J. Yang, X. J. Wang, R. Pentcheva, H. Wende, U. Bovensiepen, K. Sokolowski-Tinten, and A. Eschenlohr, arXiv:1902.05264.

[49] G. Kresse and J. Furthmüller, Phys. Rev. B **54**, 11169 (1996).

[50] J. P. Perdew, K. Burke, and M. Ernzerhof, Phys. Rev. Lett. **77**, 3865 (1996).

[51] G. Kresse and D. Joubert, Phys. Rev. B **59**, 1758 (1999).

[52] K. Dewhurst, S. Sharma, L. Nordström, F. Cricchio, O. Grnäs, E. K. U. Gross, C. Ambrosch-Draxl, C. Persson, F. Bultmark, C. Brouder, R. Armiento, A. Chizmeshya, P. Anderson, I. Nekrasov, F. Wagner, F. Kalarasse, J. Spitaler, S. Pittalis, N. Lathiotakis, T. Burnus *et al.* The ELK code, version 4.3.6, http://elk.sourceforge.net/ (2017).

[53] J. P. Perdew and Y. Wang, Phys. Rev. B **45**, 13244 (1992).

[54] U. Bierbrauer, S. T. Weber, D. Schummer, M. Barkowski, A.-K. Mahro, S. Mathias, H. C. Schneider, B. Stadtmüller, M. Aeschlimann, and B. Rethfeld, J. Phys.: Condens. Matter **29**, 244002 (2017).

[55] A. Eschenlohr, L. Persichetti, T. Kachel, M. Gabureac, P. Gambardella, and C. Stamm, J. Phys.: Condens. Matter **29**, 384002 (2017).

[56] S. Sharma, J. K. Dewhurst, A. Sanna, and E. K. U. Gross, Phys. Rev. Lett. **107**, 186401 (2011).

[57] C. Li and A. J. Freeman, Phys. Rev. B **43**, 780 (1991).

[58] H. L. Meyerheim, R. Popescu, J. Kirschner, N. Jedrecy, M. Sauvage-Simkin, B. Heinrich, and R. Pinchaux, Phys. Rev. Lett. **87**, 076102 (2001).

[59] H. L. Meyerheim, R. Popescu, N. Jedrecy, M. Vedpathak, M. Sauvage-Simkin, R. Pinchaux, B. Heinrich, and J. Kirschner, Phys. Rev. B **65**, 144433 (2002).

[60] P. Luches, S. Benedetti, M. Liberati, F. Boscherini, I. Pronin, and S. Valeri, Surf. Sci. **583**, 191 (2005).

[61] S. Valeri, S. Benedetti, and P. Luches, J. Phys.: Condens. Matter **19**, 225002 (2007).

[62] S. Colonna, A. Cricenti, P. Luches, S. Valeri, F. Boscherini, J. Qi, Y. Xu, and N. Tolk, Superlattices Microstruct. **46**, 107 (2009).

[63] R. Cuadrado and R. W. Chantrell, Phys. Rev. B **89**, 094407 (2014).

[64] B. D. Yu and J.-S. Kim, Phys. Rev. B **73**, 125408 (2006).

[65] J. I. Beltrán, L. Balcells, and C. Martínez-Boubeta, Phys. Rev. B **85**, 064417 (2012).

[66] Using ELK, Mg (IF) and O (IF) move slightly closer to the Fe plane. The variation of the z-component difference to the VASP (PBE) result is 0.009 Å for Fe-Mg and 0.010 Å for Fe-O within ELK-PBE, 0.008 Å for Fe-Mg, and 0.030 Å for Fe-O within ELK-LDA, retaining the corrugation of the IF layer for both codes and functionals.

[67] J. Ozeki, H. Itoh, and J. Inoue, J. Magn. Magn. Mater. **310**, e644 (2007).

[68] T. Bose, R. Cuadrado, R. F. L. Evans, R. V. Chepulskii, D. Apalkov, and R. W. Chantrell, J. Phys.: Condens. Matter **28**, 156003 (2016).

[69] M. Sicot, S. Andrieu, P. Turban, Y. Fagot-Revurat, H. Cercellier, A. Tagliaferri, C. De Nadai, N. B. Brookes, F. Bertran, and F. Fortuna, Phys. Rev. B **68**, 184406 (2003).

[70] K. Miyokawa, S. Saito, T. Katayama, T. Saito, T. Kamino, K. Hanashima, Y. Suzuki, K. Mamiya, T. Koide, and S. Yuasa, J. Appl. Phys. **44**, L9 (2005).

[71] E. Jal, J. B. Kortright, T. Chase, T. Liu, A. X. Gray, P. Shafer, E. Arenholz, P. Xu, J. Jeong, M. G. Samant, S. S. P. Parkin, and H. A. Dürr, Appl. Phys. Lett. **107**, 092404 (2015).

[72] M. W. Williams and E. T. Arakawa, J. Appl. Phys. **38**, 5272 (1967).

[73] D. M. Roessler and W. C. Walker, Phys. Rev. **159**, 733 (1967).

[74] R. C. Whited, C. J. Flaten, and W. C. Walker, Solid State Commun. **13**, 1903 (1973).
[75] A. Yamasaki and T. Fujiwara, Phys. Rev. B **66**, 245108 (2002).
[76] A. Schleife, C. Rödl, F. Fuchs, J. Furthmüller, and F. Bechstedt, Phys. Rev. B **80**, 035112 (2009).
[77] L. Schimka, J. Harl, A. Stroppa, A. Grüneis, M. Marsman, F. Mittendorfer, and G. Kresse, Nat. Mater. **9**, 741 (2010).
[78] J. Kang, Y.-H. Kim, J. Bang, and K. J. Chang, Phys. Rev. B **77**, 195321 (2008).
[79] J. Hamrlová, D. Legut, M. Veis, J. Pištora, and J. Hamrle, J. Magn. Magn. Mater. **420**, 143 (2016).
[80] S. Botti, F. Sottile, N. Vast, V. Olevano, L. Reining, H.-C. Weissker, A. Rubio, G. Onida, R. Del Sole, and R. W. Godby, Phys. Rev. B **69**, 155112 (2004).
[81] A. Schleife, F. Fuchs, J. Furthmüller, and F. Bechstedt, Phys. Rev. B **73**, 245212 (2006).
[82] Y.-M. Byun and C. A. Ullrich, Phys. Rev. B **95**, 205136 (2017).
[83] See Supplemental Material at http://link.aps.org/supplemental/10.1103/PhysRevB.99.195104 for animated sequences of the time evolution of the changes in the charge distribution shown in Figs. 4 and 8.